European Journal of Mechanics / B Fluids 65 (2017) 274–283

Contents lists available at ScienceDirect

European Journal of Mechanics / B Fluids

journal homepage: www.elsevier.com/locate/ejmflu

A numerical wave-maker for internal solitary waves with timely updated mass source/sink terms

Xu Wang [a,*], Jifu Zhou [a,b], Yunxiang You [c]

[a] CAS Key Laboratory for Mechanics in Fluid Solid Coupling Systems, Institute of Mechanics, Beijing, 100190, China
[b] School of Engineering Sciences, University of Chinese Academy of Sciences, Beijing 100049, China
[c] State Key Laboratory of Ocean Engineering, Shanghai Jiaotong University, Shanghai, 200240, China

ARTICLE INFO

Article history:
Received 30 November 2016
Received in revised form 7 April 2017
Accepted 12 April 2017
Available online 11 May 2017

Keywords:
Internal solitary waves
Numerical wave generation
Mass source term method

ABSTRACT

On the basis of the two-dimensional Navier–Stokes equations, a new numerical method is proposed to generate internal solitary waves (ISWs) of expected parameters by adding a source term above the interface and a sink term below the interface into the continuity equation. Fluxes between the source and the sink are balanced to assure mass conservation, and the source/sink regions (the spatial windows over which the sink/source terms are placed) are adjusted as functions of time with the interface motion. Thus, the nonphysical trailing waves can be eliminated, which makes it easy to assure the prescribed ISW parameters. Moreover, a new layout is presented to avoid the difficulty of sizing and positioning the source/sink region, which has been proved to be an intrinsic drawback of the traditional mass source method. Numerical experiments are performed to validate the proposed method by analyzing the wave displacements and vertical profiles of velocity fields. It is shown that the numerical waveform remains stable with much less trailing waves than previous methods, and the numerical results are in good agreement with theoretical and experimental results. In addition, through sensitivity analysis, a reasonable method to determine the width of source/sink region is recommended.

0. Introduction

Internal solitary waves (ISWs) are gravity waves that typically occur in stratified fluids because of the natural density stratification arising from salinity and temperature variations. A large number of observations showed that ISWs occur frequently and exist widely in most of the world's oceans [1]. There are plenty more applications of ISWs such as parameterizing their role in continental shelf energetics, their impact on marine ecology and water quality, their influence on seafloor morphology, and their implications for underwater acoustics. Specifically, ISWs have resulted in severe impacts on operation of offshore engineering structures [2]. With regard to deep-sea oil and gas exploration, ISWs have become a fundamental environmental issue, which should be considered in engineering design [3].

A two-layer representation of the ocean density stratification is a conventional approximation to study ISWs both analytically and numerically [4]. Nonlinearity and dispersion are the two fundamental mechanisms that govern the physics of ISWs. In general, nonlinearity tends to steepen a given waveform during the course of its evolution, while dispersion has the opposite effect and tends to flatten the waveform [5]. In the case of weak nonlinearity, ISWs can be described by Korteweg–de Vries (KdV) equation and extended KdV (eKdV) equation [6]. For large-amplitude models, a useful extension of the weakly nonlinear two-layer eKdV model was proposed by Miyath [7], who derived equivalent two-layer models with full nonlinearity, while retaining only the first-order weakly dispersive effects. Choi and Camassa [5] derived fully nonlinear models to describe the evolution of finite-amplitude long internal waves in a two-fluid system for both shallow and deep water configurations. Guyenne [8] computed solitary wave solutions of a Hamiltonian model for large-amplitude long internal waves in a two-layer stratification. Grimshaw et al. [9] conducted an experimental study of the effect of rotation on large amplitude internal waves. Solitary waves in continuously stratified flows have been explored with numerical solutions of the Dubreil–Jacotin–Long (DJL) equation [10]. In addition, Turkington et al. [11] presented an iterative algorithm to compute steady, translational nonlinear waves in an incompressible fluid with a stable density stratification. In particular, Dunphy et al. [12] developed a numerical tool based on DJL equation, which can produce an exact solution to the incompressible Euler–Boussinesq equations. Theoretically, it is more reasonable to consider continuous density stratification. However, the present purpose is to construct a simple and effective numerical wave-maker for investigating interactions between

* Corresponding author.
E-mail address: wangxu@imech.ac.cn (X. Wang).

http://dx.doi.org/10.1016/j.euromechflu.2017.04.005
0997-7546/

ISWs and offshore structures. The continuous density stratification will make the derivation of numerical wave-maker more complicated. Thus, the two-layer system is used as the basis for the proposed wave-maker.

To investigate ISW–structure interaction, people often have to generate ISWs in laboratory or numerically. Under laboratory conditions, an ISW can be generated in various ways such as the mixed region collapse method [13], the oscillating rod drive method [14], the piston drive method [15], and the flap drive method [16]. In numerical methods, previous ISW generation approaches are mostly implemented by imitating the laboratory wave-maker. Hsieh et al. [17] adopted the gravity collapse method in a fluid system with a density pycnocline. Lin and Song [18] constructed a two-dimensional nonhydrostatic model to study ISW generation and evolution. Shin [19] developed a numerical method to simulate internal waves by a translating and pitching foil. However, the abovementioned laboratory approaches inevitably produce obvious trailing waves at the tail of a tank. Consequently, the numerical methods imitating laboratory wave-maker techniques will also produce trailing waves. The existence of the trailing waves implies the dissipation of wave energy during wave generation. Therefore, the conventional numerical ISW generation methods are very difficult to accurately produce an expected IWS (expected waveform and amplitude).

To build an accurate and beforehand controllable numerical wave-maker for ISWs, we propose to borrow the mass source wave-generation method for surface gravity waves, which directly starts from surface gravity wave equations (e.g., Stokes wave) instead of just imitating the laboratory wave maker. As a numerical wave-generation method, the mass source term method is more flexible because the source term can be located at any position in principle. For surface gravity wave generation, many works regarding the source term method have been conducted in recent years. Lin and Liu [20] developed an internal wave-maker on the basis of the Navier–Stokes (N–S) equations by adding a mass source term. Hafsia et al. [21] constructed a two-dimensional numerical wave flume by using mass source terms and validated the accuracy of wave generation for different types of surface waves. However, there is no general rule to determine the size and position of the mass source region, which significantly affects the numerical results. Moreover, because of lack of consideration of the temporal change of the interface, the numerical waveforms often decay obviously during the initial stage of the wave propagation. Thus, we have to make some technical improvements of the source term method to apply the method to generate ISWs.

In the present paper, on the basis of the existing mass source method for surface gravity waves, a new method to generate ISWs is proposed. The new method accounts for the variations of the interface displacement and presents a new layout for the mass source/sink region to parry the difficulty of sizing and positioning the mass source region. Thus, the new method produces an expected ISW because of much less trailing waves than in previous methods.

The paper is organized as follows. On the basis of derivation of the new wave generation method, Section 1 describes the numerical models to be used. Section 2 contains comparisons of the waveform and velocity field between the numerical results by the proposed method and theoretical ones, as well as the generation process of ISWs. Finally, some conclusions are given in Section 3.

1. Numerical model

1.1. Governing equations

The present numerical method adopts N–S equations to generate ISW by adding a mass source term into the continuity equation in the source region Ω located within the computation domain. For an incompressible fluid of density ρ_i, the velocity components (u, w) in Cartesian coordinates Oxz and the pressure p_i satisfy the continuity equation and N–S equations:

$$u_{ix} + w_{iz} = 0, \tag{1}$$

$$u_{it} + u_i u_{ix} + w_i u_{iz} = -p_{ix}/\rho_i + \nu(u_{ixx} + u_{izz}), \tag{2}$$

$$w_{it} + u_i w_{ix} + w_i w_{iz} = -p_{iz}/\rho_i + \nu(w_{ixx} + w_{izz}) - g, \tag{3}$$

where g is the gravitational acceleration, the subscripts with respect to space and time represent partial differentiation, $i = 1\,(i = 2)$ denotes the upper (lower) layer fluid.

To generate ISWs by using mass source term, the mass conservation Eq. (1) is modified as follows:

$$u_{ix} + w_{iz} = \begin{cases} 0 & (x, z) \notin \Omega \\ S_i\,(x, z, t)\,/\rho_i & (x, z) \in \Omega \end{cases} \tag{4}$$

where the added mass source term $S_i\,(x, z, t)$ is a nonzero function only in the source region Ω.

1.2. Derivation for $S_i\,(x, z, t)$

In principle, any expected ISW can be generated as long as the source function is properly specified. Thus, the key point is how to design a source function $(S_i\,(x, z, t))$. If we just consider a two-layer fluid system, the mathematical relation between the source function and the waveform $\zeta\,(t)$ of an expected ISW can be derived as follows.

Fig. 1 shows the wave generation mechanism for ISW by using the mass source method, where c is the phase speed and h_1 (h_2) is the undisturbed thickness of the upper (lower) fluid layer, and the mass source region is defined as a rectangle of width 2Δ and height h(h $= h_1 + h_2$). Considering the interface fluctuation in the mass source region during the wave generation process, demarcated by ISW interface, the mass source region can be divided into two subregions (Ω_1, Ω_2), which denote the source region above and the sink region below the ISW interface, respectively. The mass source/sink terms for Ω_1 and Ω_2 are set to $S_1\,(x, z, t)$ and $S_2\,(x, z, t)$, and fluxes between the source and the sink are balanced at any time, which ensures mass conservation of the computational domain. Because the absorbing and releasing processes coexist at the left and right sides of the source/sink term region, two completely symmetrical ISW trains will be generated and propagate in opposite directions. For convenience, unless otherwise mentioned, only the rightward propagating ISW will be discussed hereafter.

The upper fluid mass released from region Ω_1 in time dt can be expressed as follows:

$$m_{out} = \int_{\Omega_1} S_1(x, z, t)\,d\Omega\,dt. \tag{5}$$

Assuming that the mass source function is dependent only on time (in other words, the mass source function $S_i\,(x, z, t)$ isuniform in Ω_i at any time), Eq. (5) can be written as follows:

$$m_{out} = S_1(t)dt \int_{\Omega_1} d\Omega. \tag{6}$$

Let us consider the rightward propagating ISW. Hence, the width of Ω_1 is Δx. Thus, $\int_{\Omega_1} d\Omega = \Delta(h1 - \zeta\,(t))$, and we have

$$m_{out} = \Delta(h1 - \zeta\,(t))S_1(t)dt. \tag{7}$$

Fig. 2 shows that after a short time interval dt, the ISW interface changes from $\zeta\,(t)$ to $\zeta\,(t + dt)$, and the wave travels a horizontal distance of $c \cdot dt$. The upper fluid mass variation dm_1 (the shaded region in Fig. 2) can be approximately expressed as follows:

$$dm_1 = \rho_1 \cdot c \cdot dt \frac{-(\zeta\,(t) + \zeta\,(t + dt))}{2}. \tag{8}$$

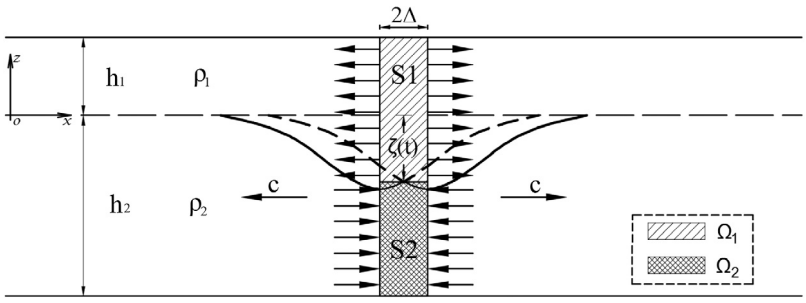

Fig. 1. ISW generation mechanism based on the mass source method.

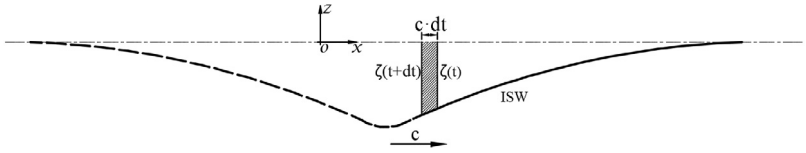

Fig. 2. Upper fluid mass variations during the generation of ISWs.

For an infinitesimal dt, we have the first-order approximation $\zeta\ (t + dt) \approx \zeta\ (t)$. Therefore, Eq. (8) can be rewritten as

$$dm_1 = -\rho_1 c\zeta\ (t)\, dt. \tag{9}$$

For any given time interval dt, the released fluid mass m_{out} from region Ω_1 is equal to the upper fluid mass variation dm_1 in the computation domain; therefore,

$$\Delta(h1 - \zeta\ (t))S_1(t)dt = -\rho_1 c\zeta\ (t)\, dt. \tag{10}$$

Thus

$$S_1\ (t) = -\rho_1 c \frac{\zeta\ (t)}{h_1 - \zeta\ (t)} \frac{1}{\Delta}. \tag{11}$$

Similarly, the mass sink function $S_2(t)$ is given by

$$S_2\ (t) = \rho_2 c \frac{\zeta\ (t)}{h_2 + \zeta\ (t)} \frac{1}{\Delta}. \tag{12}$$

1.3. Boundary and initial conditions

The top and bottom of computation domain are required to satisfy the following boundary conditions:

$$w_1|_{z=h_1} = 0,\ w_2|_{z=-h_2} = 0. \tag{13}$$

According to the continuity of normal velocity and pressure, the boundary conditions at the interface ($z = \zeta\ (t)$) are given by

$$\zeta_t + u_1\zeta_x = w_1,\ \zeta_t + u_2\zeta_x = w_2,\ p_1 = p_2. \tag{14}$$

The computation domains are exactly symmetrical, and only the rightward propagating ISWs are studied. Therefore, the left boundary can be set to a symmetry boundary condition.

The right boundary is specified as a smooth nonslip wall. To avoid wave reflection at the end, a dissipation region is applied to dissipate ISWs in the numerical flume, which is realized by adding a source term into the momentum transport equation in the vertical direction. Hence, Eq. (3) can be rewritten as follows:

$$w_{it} + u_i w_{ix} + w_i w_{iz} = -p_{iz}/\rho_i + \nu\,(w_{ixx} + w_{izz}) - g - \delta\ (x)\ w \tag{15}$$

where the damping function $\delta\ (x)$ is nonzero only in the dissipation region, otherwise $\delta\ (x) = 0$.

In the present paper, we choose a linear expression for $\delta\ (x)$

$$\delta\ (x) = \xi \frac{x - x_s}{x_e - x_s}, \tag{16}$$

where ξ is an empirical coefficient and we choose $\xi = 9.0$ here, x_s and x_e denote the horizontal coordinates of the beginning and end points of the dissipation region, respectively.

At the initial moment, there is no wave or current motion in the computation domain, which implies that both the velocity and the velocity gradient are equal to zero.

1.4. Interface treatment

The volume of fluid (VOF) method [22] is employed for tracking the ISW interface during the generation and propagation processes. The VOF equation is

$$\frac{\partial a_i}{\partial t} + \frac{\partial}{\partial x}\,(a_i u) + \frac{\partial}{\partial z}\,(a_i w) = \frac{s_{a_i}}{\rho_i}, \tag{17}$$

where a_i is the volume fraction of the ith phase fluid. The volume fractions of the two phases sum to unity, and the following three conditions are possible for each control volume: (1) $a_i = 0$: the cell is empty of the ith phase fluid, (2) $a_i = 1$: the cell is full of the ith phase fluid and (3) $0 < a_i < 1$: the cell contains the interface between the two fluids.

1.5. The internal solitary wave theory

To validate the proposed numerical wave-maker, besides the KdV, eKdV, and MCC (Miyata–Choi–Camassa) theory of a two-fluid system, the DJL model that can produce an exact solution to the incompressible Euler-Boussinesq equations is also employed.

As we know, the KdV equation is a classical theory to describe ISWs of weak nonlinearity and dispersion in shallow water.

$$\frac{\partial \zeta}{\partial t} + (c_0 + \alpha\zeta)\,\frac{\partial \zeta}{\partial x} + \beta\frac{\partial^3 \zeta}{\partial x^3} = 0. \tag{18}$$

With the increase in nonlinearity, it is difficult to make accurate predictions in contrast to experiments by using the KdV equation. An effective solution is to add a cubic nonlinear term in KdV equation, thereby leading to the so-called eKdV equation

$$\frac{\partial \zeta}{\partial t} + \left(c_0 + \alpha\zeta + \alpha_1\zeta^2\right)\frac{\partial \zeta}{\partial x} + \beta\frac{\partial^3 \zeta}{\partial x^3} = 0. \tag{19}$$

Under the two-layer approximation, the coefficients of the KdV/eKdV equation are given by

$$c_0 = \sqrt{g\frac{h_1h_2(\rho_2-\rho_1)}{\rho_1h_2+\rho_2h_1}}, \alpha = -\frac{3c_0}{2}\frac{\rho_1h_2^2-\rho_2h_1^2}{\rho_1h_1h_2^2+\rho_2h_2h_1^2} \tag{20}$$

$$\alpha_1 = \frac{3c_0}{h_1^2h_2^2}\left(\frac{7}{8}\left(\frac{\rho_1h_2^2-\rho_2h_1^2}{\rho_1h_2+\rho_2h_1}\right)^2 - \frac{\rho_2h_1^3+\rho_1h_2^3}{\rho_1h_2+\rho_2h_1}\right),$$
$$\beta = \frac{c_0(\rho_2h_1h_2^2+\rho_1h_2h_1^2)}{6(\rho_1h_2+\rho_2h_1)}. \tag{21}$$

Here c_0 is the wave phase speed, α, α_1, and β denote the coefficients of quadratic nonlinearity, cubic nonlinearity, and dispersion, respectively.

Eq. (19) has a traveling wave solution as follows [3]:

$$\zeta = \frac{A}{B+(1-B)\cosh^2(\lambda_{eKdV}(x-c_{eKdV}t))} \tag{22}$$

where A is the amplitude of ISWs, and

$$c_{eKdV} = c_0 + \frac{A}{3}\left(\alpha+\frac{1}{2}\alpha_1A\right), \lambda_{eKdV}^2 = \frac{A(2\alpha+\alpha_1A)}{24\beta},$$
$$B = \frac{-\alpha_1A}{2\alpha+\alpha_1A}. \tag{23}$$

The eKdV includes both a quadratic term and a cubic nonlinear term and exhibits solitary wave solutions that are bounded above by the limit of flat-crest waves [23], and the limiting amplitude is given [6] as follows:

$$A_{lim} = -\frac{\alpha}{\alpha_1}. \tag{24}$$

The MCC equations describe an ISW in the approximation of weak dispersion but with no limitation of nonlinearity. In addition, the shape of ISW is determined from the ordinary nonlinear equation for the interfacial displacement ζ (in the Boussinesq approximation)

$$(\zeta_X)^2 = \frac{3g(\rho_2-\rho_1)}{c_{mcc}^2(\rho_1h_1^2-\rho_2h_2^2)}\frac{\zeta^2(\zeta-a_-)(\zeta-a_+)}{\zeta-a_*} \tag{25}$$

where c_{mcc} is the phase velocity, and a_- and a_+ ($a_- < a_+$) are the two roots of $\zeta^2+q_1\zeta+q_2=0$, in which

$$q_1 = -\frac{c_{mcc}^2}{g}-h_1+h_2, \quad q_2 = -\frac{c_{mcc}^2}{g}-h_1h_2(c_{mcc}^2/c_0^2-1),$$
$$\frac{c_{mcc}^2}{c_0^2} = \frac{(h_1-a)(h_2+a)}{h_1h_2-(c_0^2/g)\,a}. \tag{26}$$

Fully nonlinear, rightward propagating ISWs in a frame moving at a wave speed c are governed by a nonlinear elliptic eigenvalue problem, namely the Dubreil-Jacotin-Long (DJL) equation [23]

$$\nabla^2\zeta + \frac{N^2(z-\zeta-h_2)}{c^2} = 0 \tag{27}$$

$$\zeta = 0 \quad at \quad z = -h_2h_1 \tag{28}$$

$$\zeta = 0 \quad as \quad x \to \infty \tag{29}$$

where $N^2(z) = -g\frac{d\tilde{\rho}(z)}{dz}$ is the square of buoyancy frequency, and the propagation speed c is to be determined as part of the solution. Once ζ and c are obtained, the induced velocity fields can be computed from the stream function $\psi = c\zeta$.

2. Numerical experiments and discussions

To test the wave generation method proposed above, using user-defined function redevelopment tools given by the Fluent software, a numerical flume is built to generate ISWs. For a specific numerical case, the numerical method first calculates the ISW interface displacement $\zeta(t)$ (Eqs. (18/22/25)) for the specific case, then substitutes ζ (t) in the mass source function derived (Eqs. (11), (12)), and finally excites the ISW in the source term region.

The computation domain is shown in Fig. 3, which consists of three regions: the mass source region, wave propagation region, and dissipation region. The widths of the three regions are Δ = 0.02m, L_p = 24 m and L_d = 6 m. The upper/lower fluid density in the two-layer fluid system is ρ_1 = 998 kg/m^3 and ρ_2 = 1025 kg/m^3.

Structured quad-type elements are used to ensure the mesh quality of the computational domain. In the x direction, a grid is refined to the size of λ/Nh (where Nh denotes the number of meshes within the integral wavelength $\lambda = \frac{1}{A}\int_{x_m}^{\infty}\zeta(x)\,dx$ as introduced by Koop and Butler [24] and x_m is the maximum wave displacement). In the z direction, the computational domain is divided into three areas: $-h_2 \le z < -A$, $-A \le z < 0$, and $0 \le z \le h_1$ (where A is the ISW amplitude). Local grid refinements are employed to overcome the numerical dispersion in the region of wave motion ($-A \le z < 0$), where the grid is refined to the size of A/Nv (where Nv denotes the number of meshes within this region). For the other two areas, the grids are determined by the law of geometric progression with a common ratio of 1.03 (the grid thickness of the first layer remains A/Nv, the greater the distance between the interface and the top/bottom boundary, the greater the thickness is). Thus, using these two parameters (Nh and Nv), we can easily determine the computational grid distributions.

The time iteration step is 0.001 s during the simulation. The N–S equations are discretized on the two-dimensional structured grids by using finite volume method, and appropriate numerical schemes are used to avoid the spurious effects due to numerical dispersion. In particular, the pressure implicit with splitting of operators algorithm is adopted to solve the pressure velocity coupling, the spatial gradients are discretized using the Green–Gauss node-based method and a second-order upwind scheme for VOF volume fraction. Moreover, the temporal terms are discretized using a second-order implicit scheme.

Four different numerical experiments are chosen to demonstrate the accuracy of the proposed mass source ISW generation method. As shown in Table 1, Case A, Case B, and Case D represent the weakly, medium, and strongly nonlinear ISW, respectively, and Case C is for a special situation where the designed amplitude approaches the limiting amplitude of eKdV (Eq. (24)). Some crucial issues, i.e., the accuracy of the numerical waveform and the flow field, the variation in the flow field during wave generation, the sensitivity of the mass source region width Δ, and the results of the grid-independence test are discussed in detail as follows.

2.1. Generation process of the ISW

With the variation in the mass source terms ($S_1(t)$ and $S_2(t)$), the velocity field and waveform will change. To explain the wave generation history, the velocity field and waveform variations near the source term region during wave generation for Case B are shown in Fig. 4, where the blank and solid areas on the left represent the source and sink term regions, respectively, which vary with the interface motion during the propagation. The solid lines and the vectors indicate the wave interface and induced velocities, respectively.

When t = 10 s, the mass source functions are very close to zero, namely $u_{ix}+w_{iz} \approx 0$ in the source/sink region. Hence, there is no significant change in the velocity field and the waveform.

At t = 18 s, with the increase in the source functions, the mass source $S_1(t)$ releases fluid in region Ω_1 and $S_2(t)$ absorbs fluid in

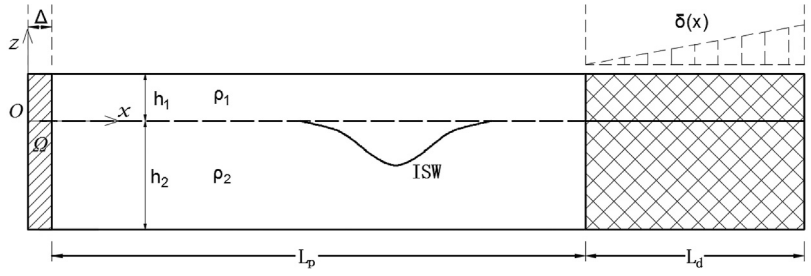

Fig. 3. Sketch of numerical flume for ISWs based on the proposed mass source ISW generation method. (Ω at the left end denotes the generation region.)

Table 1
Numerical cases.

ID	$h1$ / (m)	$h2$ / (m)	A / (m)	ISW theory	$Re\ (=\frac{\lambda U_{max}}{\nu})$	(Nh, Nv)/Grid number
Case A	0.2	0.8	0.0470	KdV	3.9e4	(80, 10)/6.07e5
Case B	0.3	0.7	0.1055	eKdV	1.1e5	(80, 10)/3.67e5
Case C	0.3	0.7	0.1780	eKdV	3.8e5	(80, 10)/1.30e5
Case D	0.2	0.8	0.2433	MCC	2.0e5	(80, 10)/3.02e5

($R_e = \frac{\lambda U_{max}}{\nu}$, where U_{max} is the maximum horizontal velocity induced by ISWs. Because of the lack of consideration of numerical viscosity, the Reynolds number may be overvalued.)

region Ω_2 gradually (see Fig. 1). Thus, the flow fields are disturbed, and the waveform is beginning to take shape.

From $t = 24$ s to $t = 30$ s, the source functions continue to increase, and the interface declines sharply. The profile of ISW is more and more apparent, and the velocity induced increases significantly during this stage.

At $t = 38$ s, the entire ISW waveform is generated. The velocity is strong at the trough and weak at the tail, which indicates that the source functions decrease from its maximum value gradually.

From $t = 38$ s to $t = 50$ s, the ISW continues to propagate rightwards, and the mass source functions gradually decrease to zero. Hence, the interface displacement near the source term region returns to zero, and the flow field decreases gradually.

2.2. Validation of waveforms

Fig. 5 shows the comparisons of the numerical interface displacements monitored at $x = 7$ m with theoretical and experimental ones under four different cases. The experiments [25] are conducted in the large-scale density stratified tank (length: 30 m, width: 0.6 m, height: 1.2 m) of Shanghai Jiao Tong University (ISWs are generated using a double-plate wave maker). For Case A, B, and D, the numerical interface displacements are in good agreement with both theoretical (the relative errors of amplitudes are within 3%) and experimental results, demonstrating that the numerical wave-maker can accurately generate the waveform whether weakly nonlinear ISW or strongly nonlinear ISW.

For Case C, which is designed to test our method for the limiting amplitude of eKdV (Eq. (24)), the comparison shows a larger difference in waveform between the theoretical and our numerical results than the above three cases, although the relative error of amplitude is not large. The reason is that the amplitude (0.1780 m) gets close to the theoretical limiting amplitude (0.1787 m), as obtained by Eq. (24) of the eKdV equation. Accordingly, the ISWs evolves flat-crested waves [26], and these waveforms are difficult to match the eKdV theory as pointed out by Dunphy et al. [12] for limiting solution of eKdV.

The numerical ISW waveforms for Case B at different times ($t = 45, 65, 85, 105$ s) are shown in Fig. 6. The results indicate that each of the numerical waveforms remains stable, and the decay of the amplitudes is weak during the propagation. From 45 to 105 s, the relative differences of the amplitude and phase are 3.30% and 0.12%, respectively.

Furthermore, we compared our numerical waveform with that of the DJL theory, which can produce an exact solution to the incompressible Euler–Boussinesq equations. The isopycnal displacement (1010 kg/m^3) at $t = 50$ s for Case B between our numerical waveform and the results calculated using the DJL equation produced by Dunphy [14] are given in Fig. 7. In addition, the numerical isopycnal displacement is also in good agreement with the results calculated using the DJL equation.

It should be noted that the proposed numerical model is based on the two-layer fluid approximation. Because of numerical diffusion, the two-layer system at beginning will evolve into a smoothing structure of the pycnocline near the interface. Fig. 8 shows the actual density profile at the ISW trough ($t = 50100$ s). Although the density distribution does not strictly confirm to the two-layer fluid approximation, the deviation is not significant. Moreover, from 50 to 100 s, the profile remains the same. These suggest that the influence of numerical diffusion is limited though unavoidable.

2.3. Validation of the velocity field

To further test the accuracy of the proposed wave generation method, the validation of velocity fields induced by ISWs is very important, especially for estimating the hydrodynamic action of ISWs on offshore structures.

The theoretical results, which are shown in Fig. 9, are based on the strongly nonlinear asymptotic approximation model in a two-fluid system of Camassa et al. [27]. The leading-order horizontal velocity dependence on z can be written as

$$\text{Upper layer fluid:}\quad u_1(X,z) = c\left[1-\frac{h_1}{\eta_1}+\left(\frac{\eta_1^2}{6}-\frac{(h_1-z)^2}{2}\right)\left(\frac{h_1\eta_1''}{\eta_1^2}-\frac{2h_1(\eta_1')^2}{\eta_1^3}\right)\right] \quad (30)$$

$$\text{Lower layer fluid:}\quad u_2(X,z) = c\left[1-\frac{h_2}{\eta_2}+\left(\frac{\eta_2^2}{6}-\frac{(z+h_2)^2}{2}\right)\left(\frac{h_2\eta_2''}{\eta_2^2}-\frac{2h_2(\eta_2')^2}{\eta_2^3}\right)\right] \quad (31)$$

where $X = x - ct$, $\eta_1' = \eta_{1X}$, $\eta_2' = \eta_{2X}$, $\eta_1'' = \eta_{1XX}$, $\eta_2'' = \eta_{2XX}$, and $\eta_1 = h_1 - \zeta$, $\eta_2 = h_2 + \zeta$.

Fig. 9(ii) shows the comparisons of vertical profiles of horizontal velocities at the ISW trough at $t = 50$ s with the theoretical and DJL equation results. In the figure, except the vicinity adjacent to

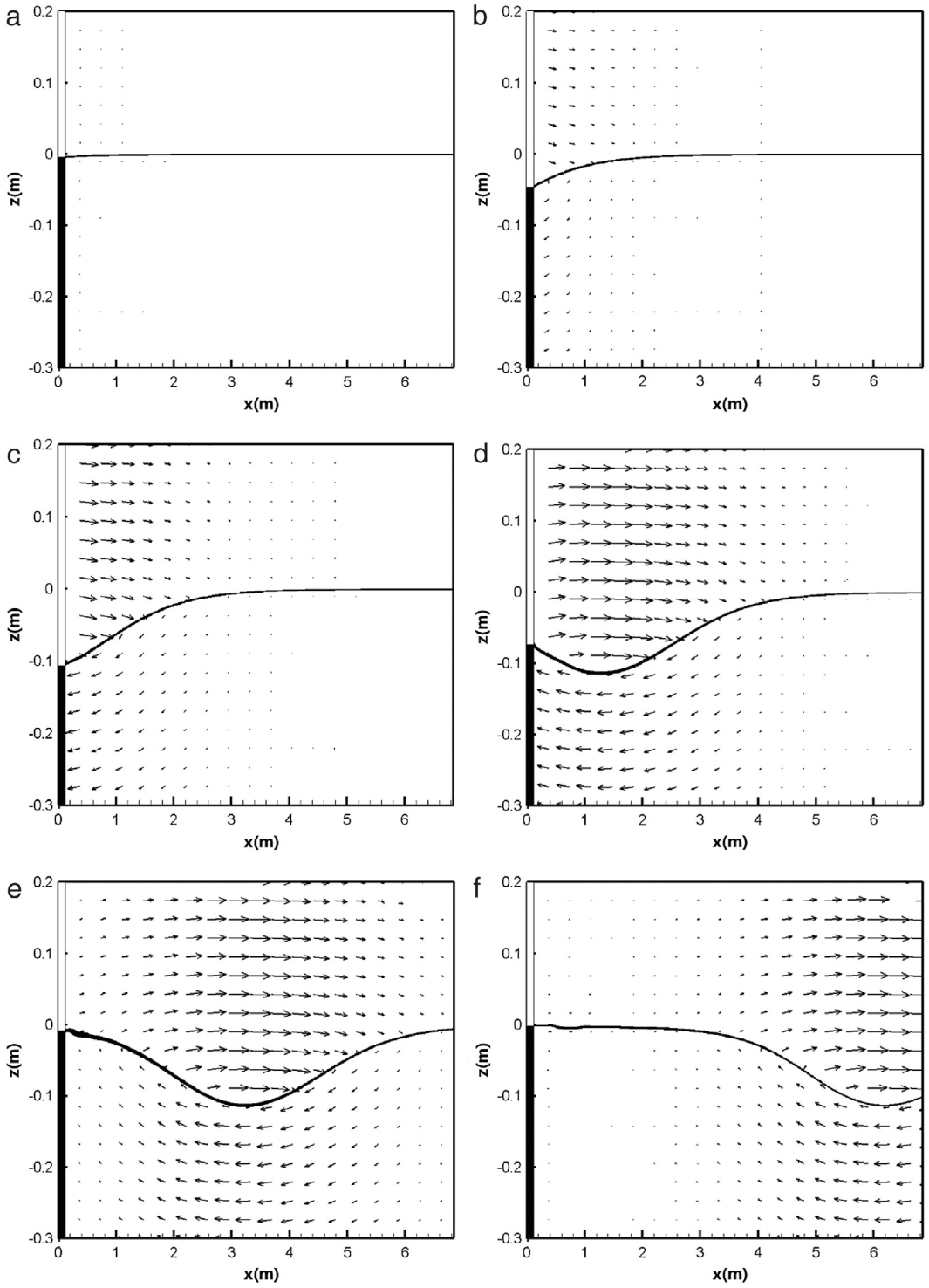

Fig. 4. Velocity fields and interface displacement near the wave generation zone at different times for Case B. (a) $t = 10$s, (b) $t = 18$ s, (c) $t = 24$ s, (d) $t = 30$ s (a) $t = 38$ s, (b) $t = 50$ s.

the interface, the vertical distributions of horizontal velocities alter little in the upper or lower fluid. Overall, the results show that velocity distributions agree well with theoretical results.

To quantitatively evaluate the error of the induced velocity field, in Fig. 9(iii), we present the numerical and theoretical variation coefficients (relative standard deviation) at different slices. The horizontal coordinates of the selected slices are as follows (shown in Fig. 9(i)): (a) $x = 9$ m, (b) $x = 8$ m, (c) $x = 7$ m, (d) $x = 6$ m, (e) $x = 5$ m, (f) $x = 4$ m, and (g) $x = 3$ m. The minimum of RMSE appears at the forepart of ISW, and its maximum appears at the wave tail. The overall variation coefficients are within 15%.

2.4. Sensitivity analysis

For a specific numerical case, the only influential factor in the proposed method is the source term region width Δ (shown in Eqs. (11), (12)). Seven numerical experiments are performed to analyze the sensitivity of Δ. These experiments are defined by

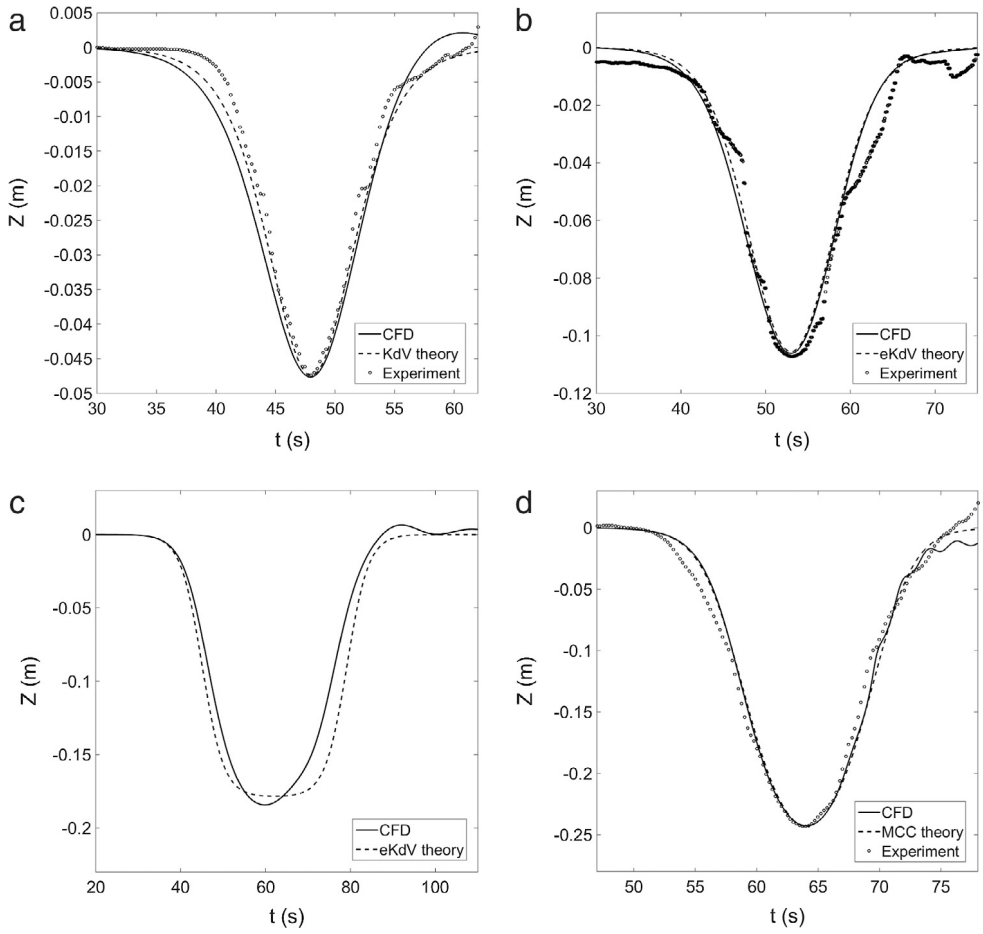

Fig. 5. Comparisons of interface displacements monitored at $x = 7$ m with theoretical and experimental ones (a) Case A, (b) Case B, (c) Case C, and (d) Case D.

$k = 0.3$, $k = 0.5$, $k = 0.8$, $k = 1$, $k = 2$, $k = 3$, and $k = 4$ (where $k = \Delta/L$ and L is the computational grid width in the wave propagation region marked by "Lp" in Fig. 3). Two dimensionless parameters (the nonlinearity $\epsilon = A/h$ and dispersion $\mu = (h/\lambda)^2$) are introduced to assess the influence of Δ.

Fig. 10 shows the comparisons of numerical results of different numerical experiments for Case B. In the figure, the symbol "•" denotes the theoretical value, and other symbols denote the numerical experimental results. The horizontal distances from the symbol "•" to other symbols represent the absolute errors of the nonlinearity between the theoretical and the numerical results. Similarly, the vertical distances represent the absolute errors of the dispersion. The relative errors of the nonlinearity between the numerical and the theoretical results are within 5%, which means the numerical amplitudes are very close to the theoretical amplitudes (refer to the definition of the nonlinearity). In addition, the relative errors of the dispersion are within 3%, which means the relative errors on the integral wavelength are also limited. These imply that the influence of Δ on numerical results is little. Although the choice of Δ seems rather arbitrary, considering the principle of mesh generation, the ratio k should not be too large or too small. For convenience, $\Delta = L$ is recommended in the proposed wave generation method.

2.5. Grid-independence test

To verify the grid independence, simulations were performed at six different spatial resolutions of Case B (amplitude: 0.1055 m), and the amplitude and phase speed measured are listed in Table 2.

Table 2
Simulated amplitude and phase speed for the grid-independence test (iteration step: 0.001 s).

Grid distribution	Amplitude (m)	Phase speed (m/s)
(20, 10)	0.0978	0.2508
(40, 10)	0.1009	0.2511
(60, 10)	0.1011	0.2511
(80, 10)	0.1019	0.2511
(80, 20)	0.1020	0.2511
(100, 30)	0.1020	0.2511

Generally, the more the grid number, the smaller is the numerical error. However, when the grid number is greater than a critical value, the error will not be significantly decreased, but the computation cost increases. In Table 2, both the amplitude and phase speed remain nearly unchanged when grids are finer than the configuration (60, 10). This indicates that the influence of grid number on numerical results is little with the configuration (80, 10) employed in the present paper.

3. Conclusions

To accurately generate a prescribed ISW in a two-layer fluid, a new numerical wave-maker is proposed based on the two-dimensional N–S equations. The method is implemented by adding a source/sink term into the continuity equation. In particular, the two regions are separated by the timely updated interface of the two fluid layers. In view of the change of the interface during the process of wave generation, the expressions for the source/sink intensity are derived. Such a new layout makes the proposed method

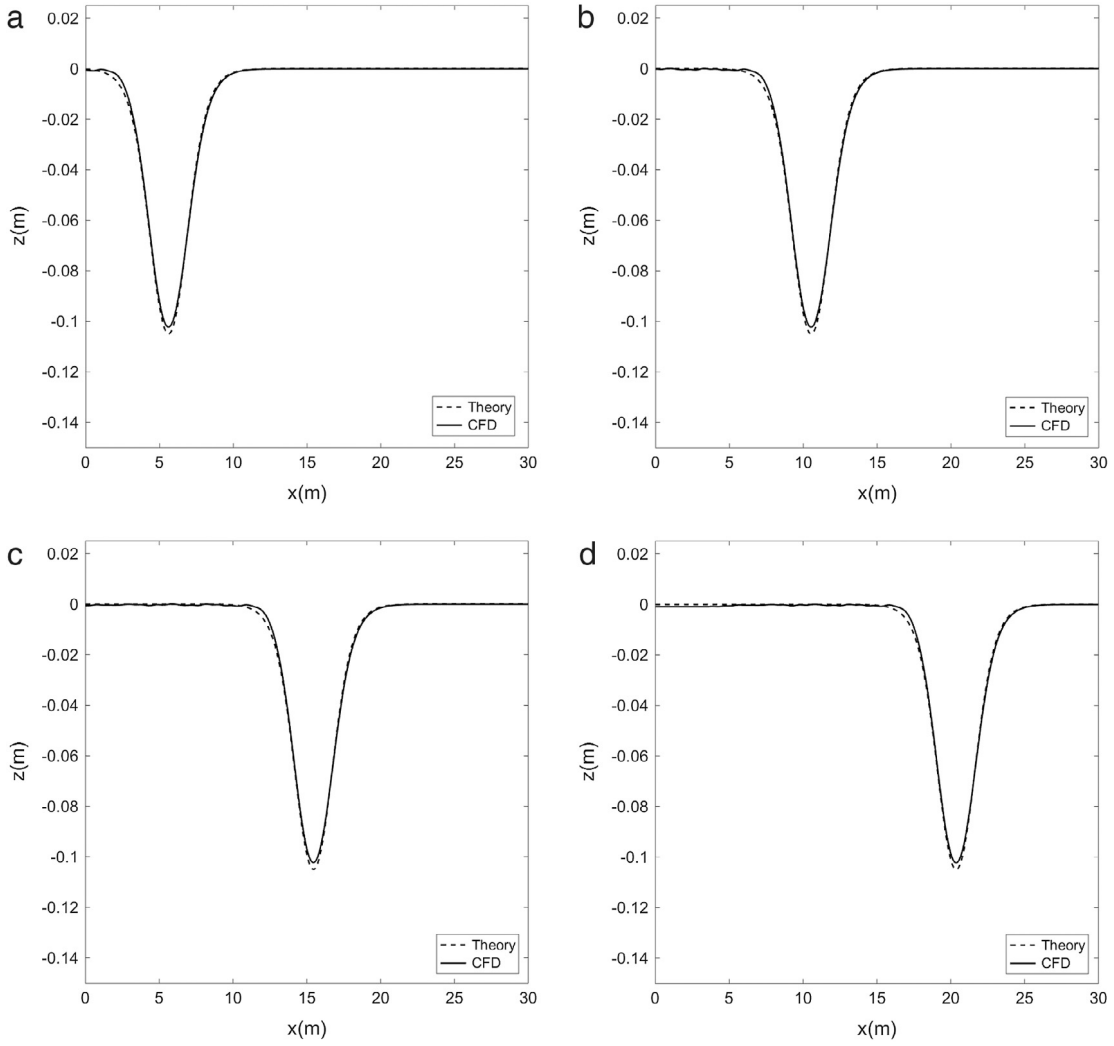

Fig. 6. Numerical waveforms at different times based on the proposed method (a) $t = 45$ s, (b) $t = 65$ s, (c) $t = 85$ s, and (d) $t = 105$ s.

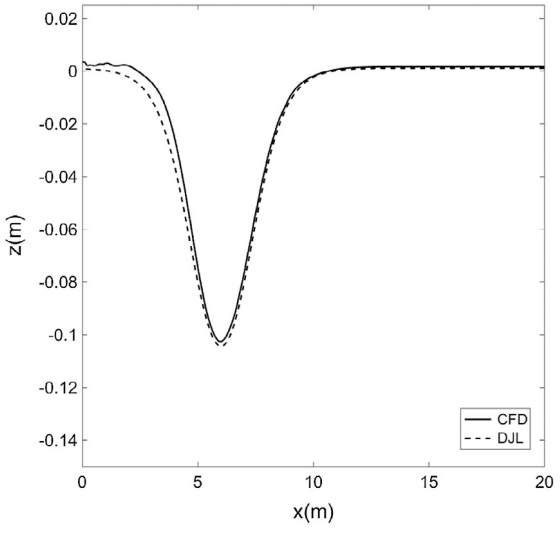

Fig. 7. Comparison of the isopycnal displacement (1010 kg/m^3) at $t = 50$ s for Case B between the simulated waveform and the calculations by the DJL.

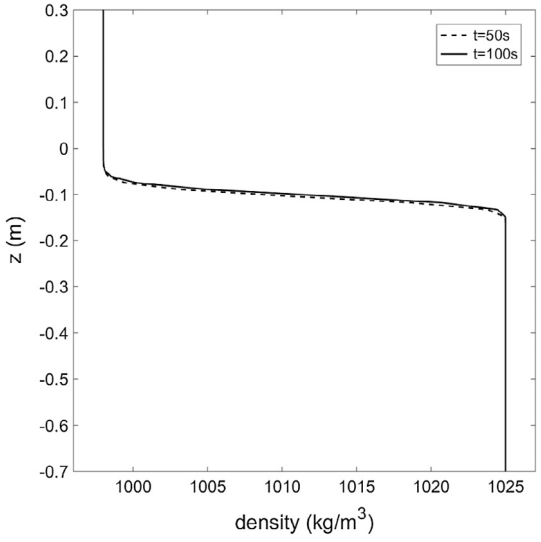

Fig. 8. Vertical profiles of density at the ISW trough ($t = 50$ s, 100 s).

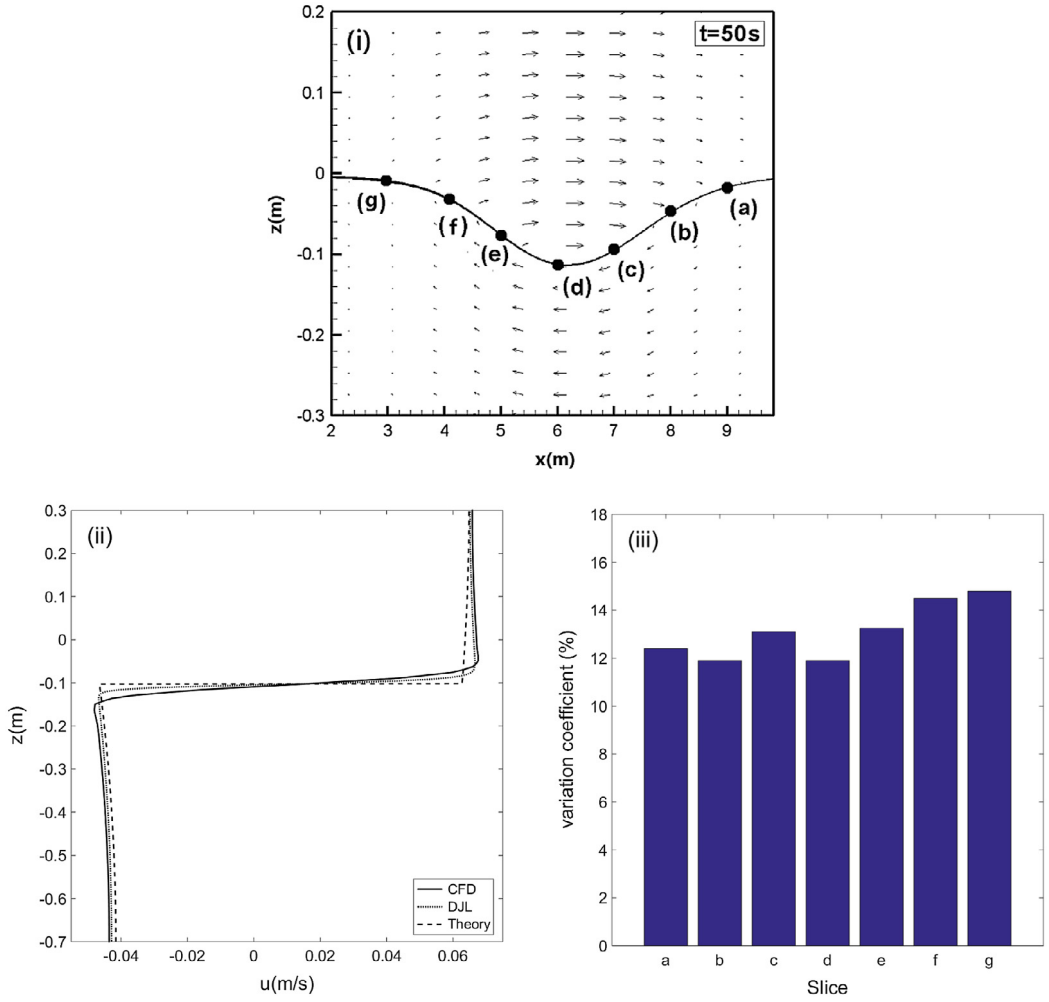

Fig. 9. Validation of the velocity field at $t = 50$ s for Case B, (i) The induced velocity field and the locations of various slices; (ii) The vertical profiles of horizontal velocities at the ISW trough; (iii) The variation coefficient of horizontal velocities at various slices.

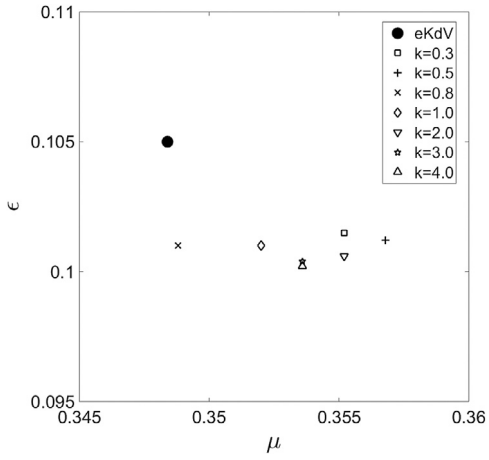

Fig. 10. Influence of the source region width Δ on numerical results.

more advantageous over the existing ISW wave generation method in that it efficiently eliminates the nonphysical trailing waves. In addition, the sizes and the positions of the source/sink can be more easily determined than the previous source mass term methods.

Different ISW cases described by KdV/eKdV/MCC equations are employed to validate the proposed method. It is demonstrated that the numerical waveforms and velocity profiles at different moments obtained by the proposed method are in good agreements with the analytical results of KdV/eKdV/MCC equations and the solution of DJL equation. Moreover, a sensitivity analysis of the source/sink region width suggests that considering it as the computational grid width in the wave propagation region is a good choice.

As an internal excitation wave generation method for ISWs, the present paper provides a new possibility to accurately investigate ISW–structure interaction.

Acknowledgments

The authors wish to thank Prof. Zhan Wang, Institute of Mechanics, Chinese Academy of Sciences, for his valuable discussions and suggestions. In addition, we thank the National Natural Science Foundation of China (11602274, 11232012, 11572332, and 11172307), 973 Program (2014CB046200), and the Strategic Priority Research Program of the Chinese Academy of Sciences (Grant XDB22040203) for their financial support to this work.

References

[1] J.R. Apel, J.R. Holbrook, A.K. Liu, J.J. Tsai, The sulu sea internal soliton experiment, J. Phys. Oceanogr. 15 (1985) 1625–1651.
[2] J.B. Bole, C.C. Ebbesmeyer, R.D. Romea, Soliton Currents in the South China Sea: Measurements and Theoretical Modeling, 1994.

[3] V. Maderich, T. Talipova, R. Grimshaw, K. Terletska, I. Brovchenko, E. Pelinovsky, B.H. Choi, Interaction of a large amplitude interfacial solitary wave of depression with a bottom step, Phys. Fluids 22 (2010) 431.
[4] J. Xie, Y. Jian, L. Yang, Strongly nonlinear internal soliton load on a small vertical circular cylinder in two-layer fluids, Appl. Math. Model. 34 (2010) 2089–2101.
[5] W. Choi, R. Camassa, Fully nonlinear internal waves in a two-uid system, J. Fluid Mech. 396 (1996) 1–36.
[6] K.R. Helfrich, W.K. Melville, Long nonlinear internal waves, Annu. Rev. Fluid Mech. 38 (2006) 395–425.
[7] M. Miyata, An internal solitary wave of large amplitude, La mer 23 (1985) 43–48.
[8] P. Guyenne, Large-amplitude internal solitary waves in a two-fluid model, C. R. Méc. 334 (2006) 341–346.
[9] R.H. Grimshaw, K.R. Helfrich, E.R. Johnson, Experimental study of the effect of rotation on nonlinear internal waves, Phys. Fluids 25 (2013) 056602.
[10] R.R. Long, Some aspects of the flow of stratified fluids, Tellus 7 (1955) 341–357.
[11] B. Turkington, A. Eydeland, S. Wang, A computational method for solitary internal waves in a continuously stratified fluid, Stud. Appl. Math. 85 (1991) 93–127.
[12] M. Dunphy, C. Subich, M. Stastna, Spectral methods for internal waves: indistinguishable density profiles and double-humped solitary waves, Nonlinear Process. Geophys. 18 (2011) 351–358.
[13] M. Carr, P. Davies, R. Hoebers, Experiments on the structure and stability of mode-2 internal solitary-like waves propagating on an offset pycnocline, Phys. Fluids 27 (2015) 046602.
[14] D. Mowbray, B. Rarity, A theoretical and experimental investigation of the phase configuration of internal waves of small amplitude in a density stratified liquid, J. Fluid Mech. 28 (1967) 1–16.
[15] J.E. Lewis, B.M. Lake, D.R. Ko, On the interaction of internal waves and surface gravity waves, J. Fluid Mech. 63 (1974) 773–800.
[16] S.A. Thorpe, On the shape of progressive internal waves, Philos. Trans. R. Soc. Lond. Ser. A Math. Phys. Eng. Sci. 263 (1968) 563–614.
[17] C.-M. Hsieh, R.R. Hwang, J.R.-C. Hsu, M.-H. Cheng, Flow evolution of an internal solitary wave generated by gravity collapse, Appl. Ocean Res. 48 (2014) 277–291.
[18] Z.-h. Lin, J.-b. Song, Numerical studies of internal solitary wave generation and evolution by gravity collapse, J. Hydrodyn. 24 (2012) 541–553.
[19] S. Shin, Simulation of two-dimensional internal waves generated by a translating and pitching foil, Ocean Eng. 72 (2013) 77–86.
[20] P. Lin, P.L.-F. Liu, Internal wave-maker for Navier-Stokes equations models, J. Waterway, Port, Coast, Ocean Eng. 125 (1999) 207–215.
[21] Z. Hafsia, M.B. Hadj, H. Lamloumi, K. Maalel, Internal inlet for wave generation and absorption treatment, Coast. Eng. 56 (2009) 951–959.
[22] C.W. Hirt, B.D. Nichols, Volume of fluid (VOF) method for the dynamics of free boundaries, J. Comput. Phys. 39 (1981) 201–225.
[23] M. Stastna, W.R. Peltier, On the resonant generation of large-amplitude internal solitary and solitary-like waves, J. Fluid Mech. 543 (2005) 267–292.
[24] C.G. Koop, G. Butler, An investigation of internal solitary waves in a two-fluid system, J. Fluid Mech. 112 (1981) 225–251.
[25] W.H. Huang, Y.X. You, X. Wang, T.Q. Hu, Wave-making experiments and theoretical models for internal solitary waves in a two-layer fluid of finite depth, Acta Phys. Sin. 62 (2013) 786–790.
[26] K.G. Lamb, B. Wan, Conjugate flows and flat solitary waves for a continuously stratified fluid, Phys. Fluids 10 (1998) 2061–2079.
[27] R. Camassa, W. Choi, H. Michallet, P.O. Rusås, J.K. Sveen, On the realm of validity of strongly nonlinear asymptotic approximations for internal waves, J. Fluid Mech. 549 (2006) 1–23.